ELSEVIER

#### Contents lists available at ScienceDirect

#### Ultrasonics

journal homepage: www.elsevier.com/locate/ultras



## Optical micro-elastography with magnetic excitation for high frequency rheological characterization of soft media

Jorge Torres <sup>a,b,\*</sup>, Antonio Callejas <sup>a,b</sup>, Antonio Gomez <sup>d</sup>, Guillermo Rus <sup>a,b,c</sup>

- a Ultrasonics Lab (TEP-959), Department of Structural Mechanics, University of Granada, Granada 18071, Spain
- <sup>b</sup> TEC-12 group, Instituto de Investigación Biosanitaria, ibs.Granada 18001, Spain
- <sup>c</sup> Excellence Research Unit "ModelingNature" (MNat), Universidad de Granada, Granada 18001, Spain
- <sup>d</sup> Department of Mechanical Engineering, University College London, London WC1E 6BT, UK

#### ARTICLE INFO

# Keywords: Optical elastography Magnetism High frequency Rheological modeling Kelvin–Voigt model

#### ABSTRACT

The propagation of shear waves in elastography at high frequency (>3 kHz) in viscoelastic media has not been extensively studied due to the high attenuation and technical limitations of current techniques. An optical micro-elastography (OME) technique using magnetic excitation for generating and tracking high frequency shear waves with enough spatial and temporal resolution was proposed. Ultrasonics shear waves (above 20 kHz) were generated and observed in polyacrylamide samples. A cutoff frequency, from where the waves no longer propagate, was observed to vary depending on the mechanical properties of the samples. The ability of the Kelvin-Voigt (KV) model to explain the high cutoff frequency was investigated. Two alternative measurement techniques, Dynamic Mechanical Analysis (DMA) and Shear Wave Elastography (SWE), were used to complete the whole frequency range of the velocity dispersion curve while avoid capturing guided waves in the low frequency range (<3 kHz). The combination of the three measurement techniques provided rheology information from quasi-static to ultrasonic frequency range. A key observation was that the full frequency range of the dispersion curve was necessary if one wanted to infer accurate physical parameters from the rheological model. By comparing the low frequency range with the high frequency range, the relative errors for the viscosity parameter could reach 60 % and they could be higher with higher dispersive behavior. The high cutoff frequency may be predicted in materials that follow a KV model over their entire measurable frequency range. The mechanical characterization of cell culture media could benefit from the proposed OME technique.

#### 1. Introduction

Micro-elastography is a subcategory of dynamic elastography that was born to map the mechanical parameters at the microscopic scale [1, 2]. This technique has been proposed as a bridge for mechanical characterization between the organ scale, where diseases are studied at an advanced stage, and the subcellular scale, where the earliest stage of diseases has been observed [3–5]. The micrometer scale of micro-elastography imposes challenging requirements that imply the need for a very fine spatial resolution. The resolution limit of the captured image stems from the capabilities of the detection system, and high speed cameras are presented as good candidates [6]. The resolution of elastography, that is, when displacements are reconstructed or velocities are estimated, has been shown to be not limited by the shear wavelength ( $\lambda$ ) of the excitation, but by the algorithms used [7,8]. However, the minimum  $\lambda$  of the propagated shear wave also plays a role in the accuracy of the final result. The relationship

between  $\lambda$  and the characteristics of the propagating medium will dictate the mechanical model to use and the assumptions to be made for the analysis. When the wavelength approaches the dimensions of the medium or the thickness of a layer, propagation is conditioned by geometry, which requires guided wave models to avoid erroneous velocity estimations [9]. Diffraction and reflection as a result of the presence of inclusions or boundaries may also generate biased velocity values and artifacts [10].

In addition, viscoelastic media are described by a complex shear modulus that is time dependent. This means that shear wave velocity is frequency dependent, and shear wave attenuation increases with frequency [11]. Viscoelastic characterization at the clinical stage is providing novel and meaningful insights into the diagnosis of pathologies and disorders [12–14]. The most widespread and direct methodology for viscoelastic characterization consists of fitting the dispersion curve

<sup>\*</sup> Corresponding author at: Ultrasonics Lab (TEP-959), Department of Structural Mechanics, University of Granada, Granada 18071, Spain. E-mail address: geresez@ugr.es (J. Torres).

(frequency-dependent response) to a rheological model. KV is one of the most widely used models due to the straightforward physical interpretation of its parameters and simplicity [15]. To achieve an optimal mechanical contrast using viscoelastic properties, reaching higher frequencies will allow to reconstruct more realistic values with a lower error [16]. Increasing the excitation frequency might result in observable volume shear waves even in submillimeter thickness layers, although the exponentially increasing attenuation over distance may result in only a few observable wavelengths before the amplitude is too low to detect it. A very recent study has shown that with a suitable setup, high frequency (>3 kHz) shear waves can be observed in phantoms and that the KV model might predict the frequency from where the waves no longer propagate (the cutoff frequency) [17].

Currently, the most widespread elastography modalities are based on ultrasound [18] and magnetic resonance [19]. In this context, most studies have focused only on the macroscale elasticity with simplified boundary conditions and linear elastic assumptions, examining large field of views at moderate resolutions. Acoustic Radiation Force (ARF)based elastography techniques have been widely used due to their real-time results and their ability to perform in vivo studies effectively [20]. But the tissue response to the impulse excitation of ARF does not contain high frequency components, generally below 1 kHz. With this,  $\lambda$  usually ranges from a few to tens of millimeters depending on the propagation velocity [2,21]. In addition, the maximum acquisition rate is generally limited to 20 kHz, and its spatial resolution is proportional to the ultrasound beamwidth, reaching hundreds of microns. In the case of magnetic resonance elastography, the resolution drops to several millimeters and the acquisition rate drops to a few hundred Hz [22]. These technical limitations have precluded the adoption of these techniques at the microscale. Early works using high speed cameras have reported significant insights into shear wave propagation at high frequencies at the microscale. In a first study, a piezoelectric transducer vibrating at 15 kHz was used for exciting an animal cell of 100  $\mu m$  diameter [23]. As a proof of concept, the authors did not consider viscoelasticity and the effect of guided waves was ignored. In a second study, they attempted to address the above problems from a physical perspective using controlled media [17]. Viscoelasticity was studied using a KV model. They created shear waves over a wide frequency range from 0.5 to 15 kHz. However, they observed inconsistent values in the KV fittings in samples with the same composition, which made it difficult to experimentally establish an accurate high frequency cutoff. Likewise, they were not able to check that the KV model fit correctly over the entire dispersion curve as they registered guided waves at the low frequency end of the measured range.

These previous studies have shown that for a micro-elastography study, an efficient method for remotely generating shear waves at high frequencies with enough amplitude away from the source, and an imaging system with sufficient acquisition rate to capture the propagation is essential. Controlling how the medium is stimulated at that scale facilitates and enhances the analysis of wave propagation. We proposed to go one step further to solve the above mentioned problems. First, a new measurement technique, called optical micro-elastography (OME), was proposed and validated. It involved a new form of wave generation that could reach high frequency using a vibrating magnetic disk embedded in a transparent medium that was excited by a transient magnetic force. A high speed camera with high resolution tracked the propagation and the displacement fields were reconstructed using optical flow algorithms. The OME technique covered from 3 kHz to the cutoff frequency. Alternative measurement techniques were also proposed to avoid capturing guided waves in the low frequency range and complete the spectrum. Dynamic Mechanical Analysis (DMA), was used to provide frequency information from 0.1 to 150 Hz. The samples were subjected to a sinusoidal strain waveform at varying frequencies in a compression machine, and the complex shear modulus was obtained. Shear Wave Elastography (SWE) cover the typical range of soft tissues, from 200 Hz to 3 kHz. Secondly, by investigating the potential of the KV

model to explain the high cutoff frequency and the agreement of the rheological behavior of soft media at different frequency ranges. The paper is organized as follows: the physical origin of the disk vibration from the magnetic force is explained; then the experimental setups for a wide frequency characterization are described, including DMA, SWE, and the proposed OME technique; after that, the OME technique is validated against simulations; finally, the phase velocity curves and the rheological behavior are presented, along with the estimation of the cutoff frequencies. The results are analyzed in the discussion.

#### 2. Theory

#### 2.1. Magnetic force on the neodymium disk magnet

Shear wave generation was achieved by applying a transient magnetic force to a disk-shaped neodymium magnet confined in a soft medium (Fig. 1a). The medium was considered diamagnetic. The magnet was placed in a fixed horizontal position below a circular air core coil and aligned with the X-axis diameter (Fig. 1b). The coil was driven with a sinusoidal time-varying voltage load  $V_{\rm coil}(t)$  that resulted in a current  $I_{\rm coil}(t)$  through the inductor, 90° out of phase with respect to the voltage (Eq. (1)).

$$V_{\text{coil}}(t) = V_{c} \sin(2\pi f_{0}t)$$

$$I_{\text{coil}}(t) = -I_{c} \cos(2\pi f_{0}t)$$
(1)

By Ampère's law, a magnetic vector field  $B_{\rm coil}({\bf r},t)$  was produced around the coil that was proportional to the total current density  $J_{\rm coil}({\bf r},t)$ , the coil cross section S and the vacuum permeability  $\mu_0$  (Eq. (2)).  $B_{\rm c}({\bf r})$  indicates the maximum time amplitude of  $B_{\rm coil}({\bf r},t)$ , where  ${\bf r}$  is the distance vector.

$$\oint B_{\text{coil}}(\mathbf{r}, t) \cdot dl = \mu_0 \iint J_{\text{coil}}(\mathbf{r}, t) \cdot dS$$

$$B_{\text{coil}}(\mathbf{r}, t) = -B_c(\mathbf{r})\cos(2\pi f_0 t)$$
(2)

 $B_{\rm coil}({\bf r},t)$  also induced an eddy current  $J_{\rm magnet}({\bf r},t)$  on the disk magnet by Faraday's law (Eq. (3)), with  $\sigma$  the electrical conductivity of the magnet. Due to its thin geometry (0.5 mm),  $J_{\rm magnet}({\bf r},t)$  was assumed to be constant along the thickness of the magnet with its flow concentric (Fig. 1c).  $I_{\rm m}({\bf r})$  indicates the maximum time amplitude of  $I_{\rm magnet}({\bf r},t)$ .

$$\oint J_{\text{magnet}}(\mathbf{r}, t) \cdot dl = -\sigma \iint \frac{\partial B_{\text{coil}}(\mathbf{r}, t)}{\partial t} \cdot dS$$

$$I_{\text{magnet}}(\mathbf{r}, t) = -I_{\text{m}}(\mathbf{r}) sin(2\pi f_0 t)$$
(3)

Ultimately, the combination of these phenomena gave rise to the Lorentz force acting on the magnet (Eq. (4)), with V the volume of the magnet. The eddy current  $J_{\text{magnet}}(\mathbf{r},t)$  in the magnet interacted with the magnetic field of the coil  $B_{\text{coil}}(\mathbf{r},t)$  creating a force perpendicular to both fields. Since the neodymium magnet had permeability close to air, its magnetic field  $B_{\text{magnet}}(\mathbf{r})$  was static and could not be altered by the magnitude of the transient fields used, allowing one to neglect the effect of this current on the magnet itself. Assuming that both materials were magnetically linear, their fields could be added and the force value enhanced. Two force components were considered.  $F'_{\text{magnet}}(\mathbf{r},t)$  was generated from  $B_{\text{coil}}(\mathbf{r},t)$ , and would be able to develop twice the frequency of the introduced transient magnetic field, while  $F''_{\text{magnet}}(\mathbf{r},t)$  was generated from  $B_{\text{magnet}}(\mathbf{r})$ , with the same frequency as the input excitation (Eq. (4)).

$$F_{\text{magnet}}(\mathbf{r}, t) = \iiint J_{\text{magnet}}(\mathbf{r}, t) \times (B_{\text{coil}}(\mathbf{r}, t) + B_{\text{magnet}}(\mathbf{r})) dv$$

$$F_{\text{magnet}}(\mathbf{r}, t) = \underbrace{\frac{I_{\text{m}}(\mathbf{r})B_{\text{c}}(\mathbf{r})}{2} sin(2\pi(2f_{0})t)}_{F'_{\text{magnet}}(\mathbf{r}, t)} + \underbrace{I_{\text{m}}(\mathbf{r})B_{\text{magnet}}(\mathbf{r}) sin(2\pi(f_{0})t)}_{F''_{\text{magnet}}(\mathbf{r}, t)}$$
(4)

An alternative expression of the force, in terms of the magnetic flux density, can be derived by using Ampère's law in its vectorial form

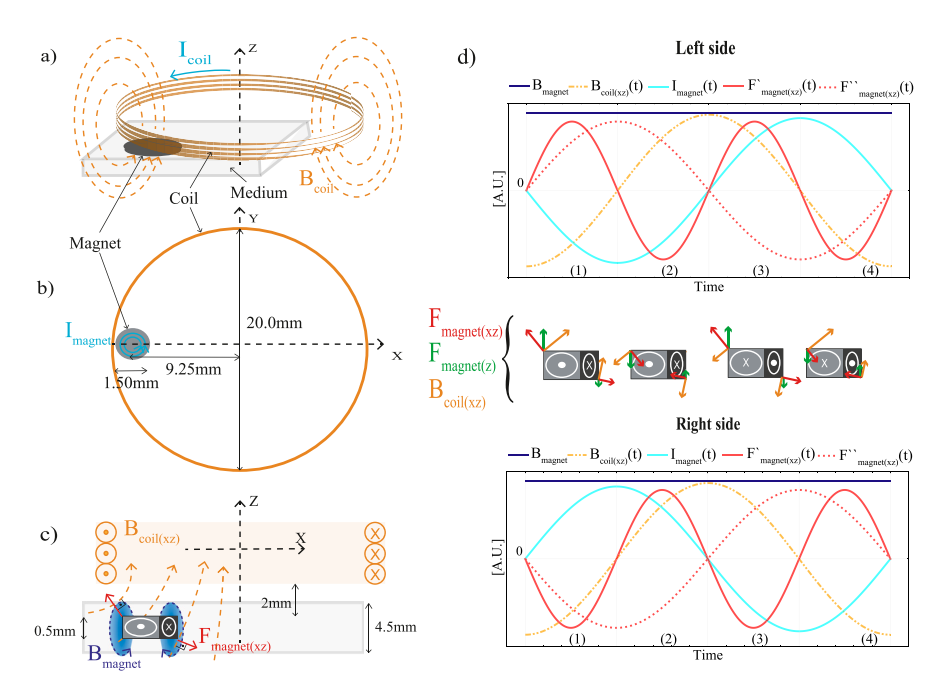


Fig. 1. Generation of a transient magnetic force after applying a sinusoidal input voltage. (a) The disk-shaped neodymium magnet receives the magnetic field of the air-cored coil. (b) The magnet is placed in a diameter coinciding with the X-axis and close to the edge of the coil. (c) The eddy current generated in the magnet  $I_{magnet}(t)$  interacts with the magnetic field of the coil  $B_{coil(xz)}$  and its own magnetic field  $B_{magnet}$ , thus producing a Lorentz force  $F_{magnet(xz)}$  perpendicular to both fields. The position of the magnet causes the forces in the XZ plane to be non-symmetrical. The equilibrium point is displaced and dominated by the side closer to the coil. (d) The fields on each side of the magnet present inverted trends, creating a pair of forces and causing the disk-shaped magnet to vibrate in a seesaw-like manner. The different gray shades distinguish the opposite polarity of the eddy current inside the magnet. Each time interval (1 to 4) represents the directional behavior of  $B_{magnet}$  (purple line),  $B_{coil(xz)}(t)$  (orange line),  $I_{magnet}(t)$  (cyan line),  $F'_{magnet(xx)}(t)$  and  $F''_{magnet(xx)}(t)$  (red lines) after the harmonic excitation.

(Eq. (5)) [24]. Considering only the effect on the z axis and being C a constant depending on magnetic parameters and the volume of the magnet, we concluded that the force was proportional to the spatial gradient of  $B_{\rm coil}$ . This expression was used to find the optimal location of the magnet in the z axis. As shown in the results section, the spatial gradient was higher just outside the coil. That was why the magnet and the medium were placed just outside, as observed in Fig. 1c.

$$F_{\text{magnet}}(z,t) = C \left( B_{\text{coil}}(z,t) \frac{\partial B_{\text{coil}}(z,t)}{\partial z} + B_{\text{magnet}}(z,t) \frac{\partial B_{\text{coil}}(z,t)}{\partial z} \right)$$
 (5)

These equations explain how it was possible to get the magnet to act as a shaker and generate shear waves. The magnitude in each direction of the  $B_{coil}(\mathbf{r},t)$  field depended on the position. When the magnet was near the edge of the coil, the dominant component was  $B_{coil(x)}$  with a moderate contribution of  $B_{\mathrm{coil}(z)}$ , as shown in Fig. 1c. These components coupled with  $I_{\mathrm{magnet}(y)}$  to generate  $F_{\mathrm{magnet}(xz)}$  (Fig. 1d). Due to the rapid change in polarity of the magnetic field and the opposite directions of current within the magnet, a pair of forces was generated, thus simulating a simple lever motion. However, the pivot point was closer to the right end because the force was not perfectly symmetric and its magnitude was greater closer to the coil. This is shown in Fig. 1d with larger circles indicating a higher eddy current on the magnet. This decompensation could try to move the magnet in the XY plane, but since it was confined, this motion was constrained. The rest of the force components had a very low magnitude. If the magnet were aligned with the Z-axis shown in Fig. 1, most of the  $B_{coil}(\mathbf{r},t)$  flux lines that would pass through the magnet would be vertical  $(B_{coil(z)})$  and therefore the value of  $F_{\text{magnet}(z)}$  would be significantly reduced.

#### 3. Methods

#### 3.1. Experimental setups for a wide frequency characterization

The remote transient magnetic force produced by the coil induced the generation of high frequency shear waves by a disk-shaped magnet, as explained in Section 2. The permanent magnet was made of neodymium (NdFeB-45) with 1.5 mm of diameter and 0.5 mm of thickness. The circular coil was made of copper with a wire diameter of 0.5 mm, 75 turns, inner diameter of 20.0 mm, and 12.5 mm of height. This resulted in a very low inductance of 0.1 mH. Low inductances are an advantage because more current will be induced in the coil at the same voltage. The chosen excitation was a linear frequency sweep (chirp) from 5 to 22 kHz, coming from a waveform generator (33500B Series, Keysight, California, USA) that after power amplification (7224, AE Techron, Indiana, USA) reached 200 Vpp. The magnetic field  $B_{\rm coil}$  at different frequencies was characterized experimentally by using Faraday's law of induction with a pickup coil, made with 10 turns and 10 mm diameter. This second coil captured the electromotive force at different positions along the Z axis of the main coil.

A high-speed camera (FastCam SA-Z, Photron, Japan) was the core of the imaging section. It had installed a 12x zoom lens (Navitar, New York, USA) from which we acquire  $640\times360$  images with  $10\times10~\mu\text{m}^2$  pixel resolution at a frame rate of 80 kHz. This ensured compliance with the Nyquist criterion. The camera lens was aimed at a 45° reflecting prism that held the medium and allowed us to study the horizontal plane of propagation (Fig. 2b). A fiber-coupled halogen light source (OSL2, Thorlabs, Inc., New Jersey, USA) with a collimation attachment provided adequate stable continuous lighting. The camera sent a trigger to the waveform generator to ensure synchronization. All elements were placed in independent structures to avoid unwanted vibrations (see Fig. 2).

The camera tests provided data to reconstruct the dispersion curve in the high-frequency range. To cover the low frequency range of the dispersion curve, we used a Verasonics research system (Vantage 256, Verasonics Inc., Redmond, WA, USA) to perform Shear Wave Elastography (SWE) [25]. To remotely produce shear waves, an ARF push of 1000 cycles [26] was applied to the medium with an L11-5v linear probe (Fig. 2f). The central frequency was 7.6 MHz. The focal distance was set at 25 mm. Immediately after, ultrafast imaging was performed using plane waves with an acquisition rate of 12.5 kHz.

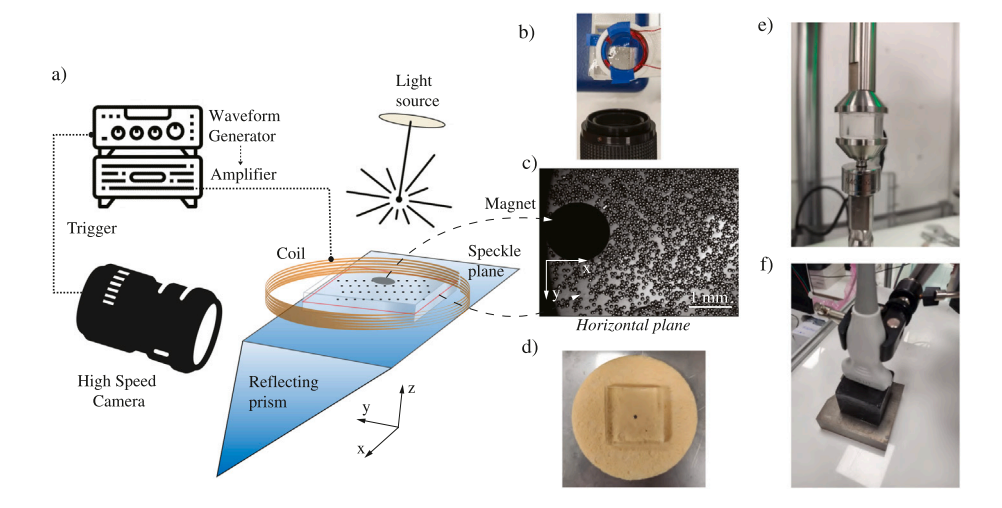


Fig. 2. Experimental setups for mechanical characterization. (a) The medium is placed on a reflecting prism in contact with its larger surface allowing horizontal positioning of the high-speed camera. (b) A picture taken from the position of the light source. The light is also reflected in the prism to directly reach the camera lens. (c) Image captured by the camera of the speckle plane (XY). The disk-shaped magnet is displayed in total black. (d) Transparent sample fabricated for the OME test. (e) DMA frequency sweep test with cylindrical sample. (f) SWE experiment with cubic sample.

To remove the effect of random noise, 10 consecutive frames were averaged.

Finally, a DMA experiment on an ElectroForce 3200 (TA Instruments, EEUU) device completed the lower end of the frequency spectrum. A cylindrical sample was placed between two planar plates. The lower plate was attached to a load cell whose maximum capacity was 22 N, with a resolution of 0.001 N (Fig. 2e). Frequency sweep tests were conducted to obtain the complex modulus of the samples. The displacement was controlled by moving the upper plate. Before starting the measurements, to ensure an even contact, a ramp load was applied until 1 N was reached. Oscillatory compression loads with stepped values from 0.1 to 150 Hz with a dynamic amplitude of 0.05 mm were carried out. The software performed a Fourier analysis to obtain the real and imaginary components of the complex modulus, the storage and the loss modulus, respectively. The acquisition rate was 10 kHz.

#### 3.2. Sample preparation

For each measurement technique, DMA, SWE, and OME, hydrogel samples with a different geometry were fabricated. The hydrogel was manufactured with polyacrylamide (PAM), a polymerized material with two useful properties. First, varying the concentration of PAM allowed tuning the viscoelastic properties. Second, the medium was completely transparent, which was necessary for light to pass through and allow visualization by the camera. A previous recipe mimicking the acoustic properties of biological tissues was adapted to manufacture PAM with these requirements [27,28]. Acrylamidebis solution (19:1 bis ratio, 40% solution, OmniPur) was reconstituted by mixing with distilled water and glycerol 10% (v/v) in a conical tube. We considered three different concentrations of PAM to have a variety of mechanical responses, namely 20%, 30% and 40% (v/v). To initialize the polymerization of PAM, Ammonium Persulfate (APS 98%, Sigma Aldrich), 0.5% (v/v) of 10% (w/v) was added and mixed until homogenization. N,N,N',N'-Tetramethylethylenediamine (TEMED 99%, ReagentPlus) was added 0.2% (v/v) as a catalyst to accelerate gel polymerization. All materials were supplied by Merck (Merck KGaA, Darmstadt, Germany).

For a successful visualization of the shear waves, the addition of optical speckles using particles smaller than the wavelength was required. Glass beads with diameter of 75  $\mu m$  (Model 59200U, Supelco) were added to form a single plane within the sample to ensure high image contrast and to avoid the observation of out-of-plane displacements.

The procedure had a duration of 40–60 s and was conducted as follows. A first layer of PAM mixture was poured into a rectangular mold shortly after TEMED was added. During the polymerization process, it was observed that as the medium solidified, a thin liquid layer formed on top of it. At this point, glass beads were placed, forming a homogeneous distribution on the surface, after passing through a 100  $\mu$ m mesh sieve. Then the neodymium disk was placed on the same plane. Finally, the second layer of PAM was poured and began to diffuse into the first layer. The molecules in the two layers began to interact, causing the layers to merge. The images taken by the camera (Fig. 2c and d) show that both the particles and the disk were on the same plane. Similarly, a homogeneous propagating wavefront during displacement reconstruction confirmed that the layers were merged. The resulting medium had a 20  $\times$  20 mm² surface and a thickness of 4.5 mm. 3 samples were made for each PAM concentration.

To study the combined spatial resolution of the imaging and excitation systems for high frequency waves, bilayer samples were fabricated. They were composed of two vertically divided layers with different PAM concentration. The left layer had a 40% concentration of PAM, while the right layer had a 20% concentration. The procedure was similar to that explained above. In this case, each layer was subdivided into two parts for each concentration, which eventually merged. The neodymium disk was placed in the 40% part.

The samples used for the SWE control experiment followed the same fabrication procedure. The cubic mold used had dimensions of  $50 \times 50 \times 50 \text{ mm}^3$  to avoid reflections or guided waves in our analysis. It consisted of a single layer with graphite powder (Pressol Schmiergerate GmbH, Germany) for acoustical scattering instead of glass beads. For the DMA experiment, the cylindrical mold had 20 mm of diameter and 12 mm of height. No scattering particles were required. Magnets were not embedded in the sample for DMA and SWE (see Fig. 2e,f).

#### 3.3. Displacement and phase velocity reconstruction

To obtain a dispersion curve that provided a consistent wide frequency characterization, the results of the three techniques used, DMA, SWE, and OME, were combined to obtain values from the quasi-static range to the cutoff frequency.

The camera was only able to capture the displacements of the particles on the horizontal plane (XY). However, the alternating motion of each side of the magnet took place in a perpendicular plane (see Fig. 4a). This motion sheared the surrounding medium and the

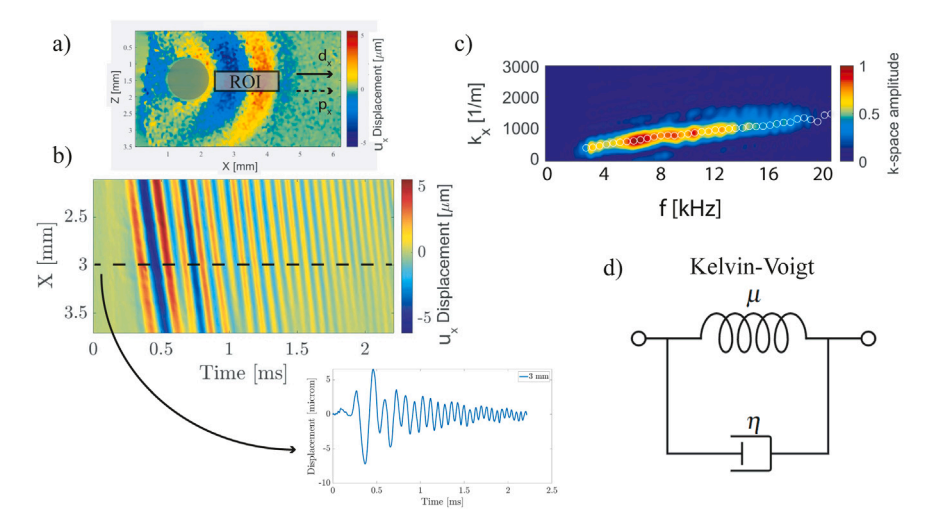


Fig. 3. High frequency data reconstruction of longitudinal waves in a 40% PAM sample. (a) Displacement map estimated using a dense optical flow algorithm. The propagation direction  $d_x$  and the particle polarization  $p_x$  was parallel. (b) Spatiotemporal displacement profiles of the horizontal component  $(u_x)$  averaged in depth taking the Region of Interest (ROI) indicated. The graph below displays the temporal displacement profile at 3 mm. (c) 2D Fourier transform of the displacement profiles with highest energy points detected for each frequency. (d) Kelvin–Voigt rheological model scheme that was used for viscoelastic characterization.

diffracted transverse shear waves coming primarily from the borders of the magnet disk created a new propagation front due to the displacement component in the horizontal direction  $(u_x)$  [29]. This led to the generation of longitudinal shear waves in the speckle plane that the camera could detect as a sequence of frames that formed a wave propagation movie.

A dense optical flow algorithm was used to estimate 2D displacement maps [30]. Ideally, each pixel in the frame was assigned a displacement value. However, the spatial resolution was reduced in favor of a more robust and smoother result. The size of the pixel neighborhood was 5, which worsened the spatial resolution from  $10 \times 10$  to  $50 \times 50 \, \mu \text{m}^2$ . A spatial Gaussian filter of size 10 pixels was also applied, for noise reduction and better detection of fast motion. Note that this filter did not change the spatial resolution. Only the lateral propagating component was considered, corresponding to the X-axis (see Fig. 3a). Before velocity estimation, a region of interest (ROI) to the right of the emitting disk was taken. The ROI dimensions were 2 mm in the lateral dimension, and 0.5 mm in the depth dimension, aligned with the center of the disk. To reduce random noise and computation time, displacement time profiles were averaged over ROI depth (Z-axis), and time upsampled by cubic interpolation (see Fig. 3b). For the bilayer samples we also applied a spatial directional filter to keep only the forward propagation direction [10].

In the SWE part, the Verasonics system provided the beamformed IQ data with which particle motion can be estimated using the Loupas correlation algorithm [31]. An ROI of dimensions  $10\times10~\text{mm}^2$  was taken to the right of the push. The same pre-processing as with OME was used here.

The dispersion curve can be obtained with the 2D Fourier transform. The reconstructed spatiotemporal data was converted to the frequency domain, also called the (f,k) space (Fig. 3c). The highest energy propagation mode was identified by finding the pairs of wavenumber k (spatial frequency) and frequency f (temporal frequency) related to the peak values of the (f,k) space amplitude. No amplitude mask was used to explore the maximum frequency information. The shear wave phase velocity for each frequency was obtained directly as  $c_s = f/k$  [32]. The characterization of the viscoelastic properties of the medium was carried out by fitting the theoretical expression of the shear wave phase velocity  $c_s(f)$  according to the KV model (Fig. 3d) to the experimental dispersion curve [33]. To obtain the shear elasticity  $\mu$  and viscosity  $\eta$  the BFGS nonlinear minimization method was used. It is an iterative algorithm used for unconstrained optimization problems. It uses an approximation of the Hessian matrix to update the search direction at

each iteration [34]. The phase velocity was also calculated from DMA data, replacing the storage and loss moduli in the KV expression [33].

Finally, the potential of the KV model to explain the high cutoff frequency was investigated. According to Holm [35], in the low frequency regime ( $\omega \tau < 1$ ) elasticity dominates over viscosity and waves propagate, being  $\tau = \eta/\mu$  the relaxation time, and  $\omega$  the angular frequency. As the frequency increases, the viscous term ( $\omega \eta$ ) gets closer to the elasticity term ( $\mu$ ) and waves are strongly attenuated, and the physical phenomenon approaches to the solution of a diffusion equation. Setting the observable propagation limit in  $\omega \tau = 1$ , the theoretical cutoff frequency is calculated as  $f_c = \frac{1}{2\pi \tau}$ .

#### 3.4. FDTD model

A 2D finite difference time domain (FDTD) model was used to validate the velocity estimated from the propagation of longitudinal shear waves created from the vibration of the magnet disk. The mechanical wave propagation problem was solved numerically based on previous work of the group [36,37] using the Matlab programming environment (R2018b, The MathWorks Inc., Natick, MA, USA). The governing equations, namely dynamic equilibrium, kinematic, and constitutive, were implemented considering a KV viscoelastic model.

A 3D model would be required since the excitation and the mechanical response were distributed perpendicularly to each other. However, this would entail a high difficulty in reproducing the excitation coming from the magnetic field, as well as several diffraction artifacts near the borders, which would be out of the scope of the study. To simplify this complexity and reduce computational load, a 2D numerical study was performed in the lateral plane (XZ), focusing on the midplane. The geometry consisted of a 2D rectangular medium with an embedded rectangular magnet element located in its center. The model considered a staggered grid for spatial discretization of the variables. Free boundary conditions were established for all edges of the propagation medium, with the exception of the bottom edge that was fixed (Fig. 4c). The neodymium magnet was modeled as a solid elastic material. The excitation was an angular displacement that was prescribed in the right corner of the magnet. The real excitation could not be fully reconstructed by looking at the lateral plane with the camera. This was due to the fact that the light had to pass through 20 mm of material. Therefore, we used as excitation the output signal of the generator scaled by the initial rotation of the magnet, which was observable. Also, the magnet was fixed at a point to the right of its vertical median

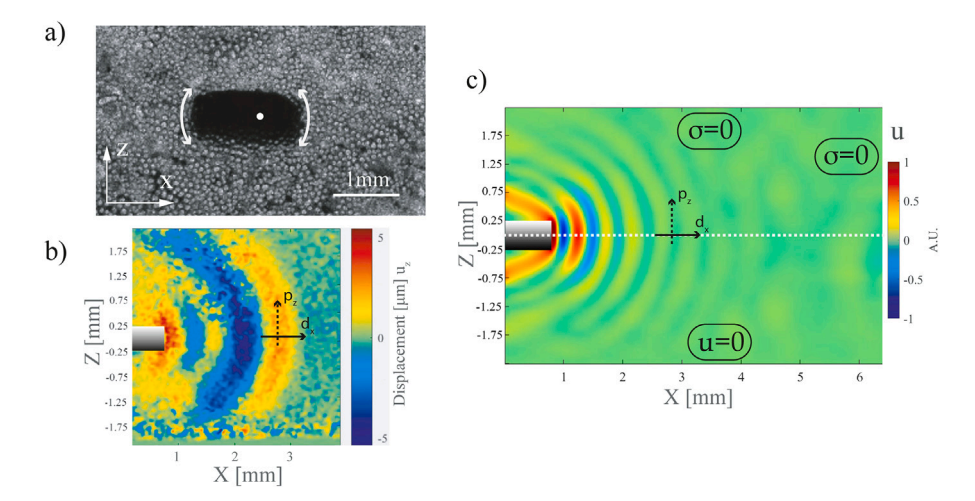


Fig. 4. (a) Lateral view (XZ) showing the transient alternating magnet motion. The magnet is fixed on the white point due to the alternating magnetic forces. (b) Reconstructed experimental vertical displacements  $(u_z)$  showing consecutive wavefronts at 0.6 ms after the beginning of magnet motion in the lateral plane of propagation (XZ). (c) Geometry and map of the vertical particle displacements  $(u_z)$  of the right side of the simulation model (FDTD) at 0.6 ms after the beginning of magnet motion.  $\sigma = 0$  indicates free border, while u = 0 indicates fixed border. The particle displacement  $p_z$  was perpendicular to the propagation direction  $d_x$ .

Table 1
Values of the parameters for all the cases simulated by using the FDTD model.

Parameter	Description	Value
xS	Horizontal dimension of the domain	20 mm
zS	Vertical dimension of the domain	4.5 mm
$\Delta x$	r spatial step	20 μm
$\Delta z$	z spatial step	20 μm
$\Delta t$	Time interval	5e-9 s
$t_T$	Total time of simulation	2.5 ms

plane because of the non-symmetrical magnetic field (see Fig. 4a). The distance was obtained from magnetic simulations (see Fig. 5e).

The material properties of the medium were inferred from the fitting of the KV parameters with the OME results, shown in Table 2. The compressional modulus K was estimated assuming  $K = c_p^2 \rho$  [38], where  $c_p = 1540$  m/s is the speed of sound and  $\rho = 1000$  kg/m³ the density of PAM [27]. The volumetric viscosity parameter  $\eta^p$  was neglected. Notice that this simplification would overestimate the absolute amplitude in the simulations compared with the and high speed camera observations. However, since the objective of the simulations was to validate the experimentally estimated velocity values, the absolute amplitude information was not relevant. The dimensions and parameters of the discretization model are summarized in Table 1. To obtain the phase velocity, the same reconstruction algorithm described in Section 3.3 was applied. The horizontal component of the displacement  $u_x$  was taken, which theoretically should have the same velocity as the longitudinal shear waves captured by the camera (white midline in Fig. 4c).

Fig. 4b shows the experimental displacement reconstruction in the lateral plane (XZ) of a 40% PAM sample. When the magnet disk sheared the medium, the vertical displacement component  $u_z$  created transverse shear waves in this plane. The amplitude of these shear waves was similar to that of the longitudinal shear waves, but due to low light conditions and poor image quality, the result was noisier compared to the XY plane. Still, a comparison with the displacements of the simulations showed that there was a qualitative agreement between them. The observations confirmed that the magnet vibrated as a simple lever, which was in agreement with the expected behavior foreseen in Section 2.

#### 4. Results

#### 4.1. Magnetic field and force optimization

Magnetic characterization was performed using the Finite Element Method Magnetics (FEMM v4.2) software [39]. An axisymmetric problem was defined with the geometry and material properties previously described. At 5 kHz, with an input voltage of 200 V, the current was 60 A. The magnetic flux density peaked at 0.31 T where the X-axis intersected the coil (Fig. 5a). Near the top surface of the magnet  $B_{r}$ was 0.14 T. The permanent magnetic field of the magnet reached a maximum of around 800 mT at its edges (Fig. 5b). In Fig. 5c the measurements taken by the pickup coil of  $B_{r}$  along the Z axis validated the simulation results. As described in the theory section (Eq. (5)) the magnetic force in the z axis is proportional to its spatial gradient. Thus, the magnet was placed near the edge of the coil where the magnetic force was maximum (Fig. 5d). The time behavior of the Lorentz force showed some deviation from the generator output because of the double frequency term that the coil added (see Fig. 5e). The inductive impedance increased with frequency, which meant that a lower current developed. Therefore, the magnitude of  $F_z$  attenuated over time as the excitation chirp changed frequency. The attenuation factor was proportional to the recorded displacement. To find the position on the magnet where  $F_z$  changed direction, we searched for the sign change of  $J_{\text{magnet}}$ , assuming a constant value in its thickness. It was found approximately 1 mm from the left side (the edge closest to the coil, the green part). This distance was used in the wave simulations.

### 4.2. OME results and experimental dispersion curves combining with DMA and SWE

The dispersion curves in the high frequency range (HF  $> 3\,$  kHz) obtained by OME are presented for each PAM concentration in Fig. 6a. The frequency information started around 3 kHz up to the estimated high cutoff frequency. This upper limit was observed at the point where information about the highest energy propagation mode in the (f,k) space was no longer available. It was noticed that as the PAM concentration of the sample increased, the recovered velocity information reached higher frequencies. For 40% the response reached a frequency of 20.2 kHz, for 30% it is up to 15.3 kHz, and for 20% up to 9.8 kHz. Therefore, ultrasonic shear waves were generated and captured. The phase velocities coming from the simulation displacement data (FDTD) are also displayed. They are mostly superimposing on the OME data.

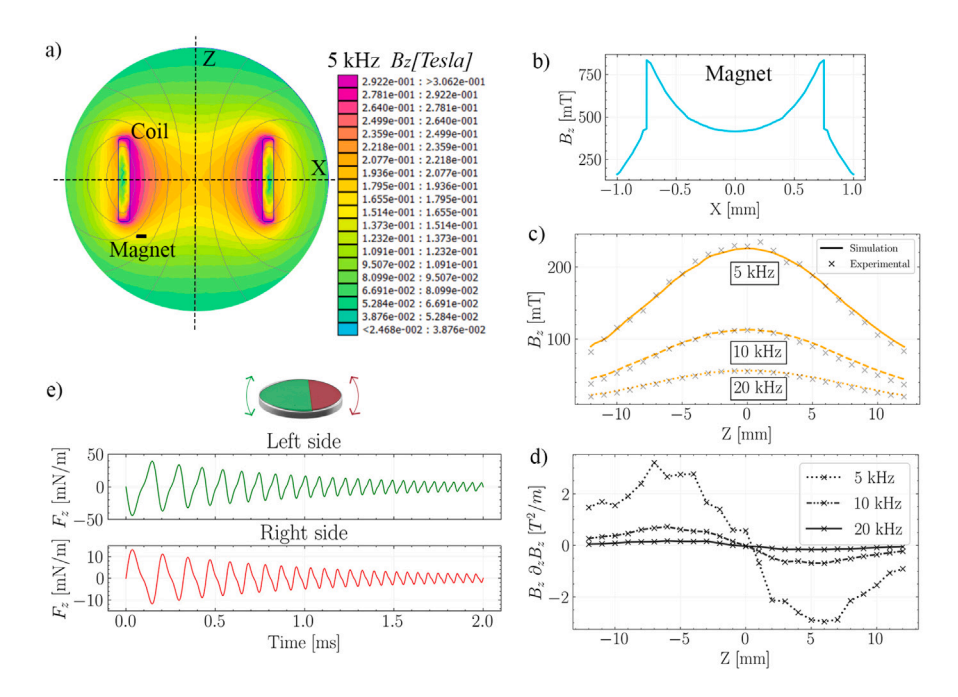


Fig. 5. Magnetic simulation results. (a) Magnetic flux density generated by the coil at 5 kHz. (b) Static magnetic field of the neodymium magnet that is added to the field coil. (c)  $B_z$  measured experimentally along the central vertical axis Z with the simulated values. (d) Spatial gradient in the z axis of the coil magnetic field. (e) Time evolution of the Z component of the Lorentz force on the upper face of the magnet.

This proved that in a KV medium, the magnet lever motion was capable of generating longitudinal shear waves in the observed frequency range. It was also emphasized that, since the velocities were of a few m/s, they belonged to shear waves. The right inset in Fig. 6a displays the exploitable frequency content of each PAM concentration. It can be seen that the frequency information is comparable to the cutoff obtained with the phase velocity. In the case of 40%, the energy is spread over a wider frequency range, which may cause the wavy shape and the jumps seen in the phase velocity.

The low frequency range (LF < 3 kHz) was the combination of DMA and SWE (Fig. 6b). For SWE the frequency information started at 200 Hz and ended at 3 kHz for the 20% concentration, in the case of 30% it went up to 3.8 kHz and for 40% up to 4.5 kHz. For all of them, 3 kHz was established as their upper limit for a consistent comparison. In this range, a higher concentration of PAM implied a more noticeable dispersion response. The DMA values ranged from 0.1 to 150 Hz with phase velocities in line with those of SWE. The frequency axis in Fig. 6b is represented in log scale. Furthermore, storage G' and loss modulus G'' are shown in a log–log scale in the upper inset. In this frequency range G' was one order of magnitude higher than G''. All techniques provided consistent values with each other without significant jumps between them.

#### 4.3. Rheological behavior and cutoff frequencies

Table 2 shows the KV fitted parameters for each frequency range, including the whole frequency range as WF = LF + HF. For the study of the goodness of fit, the mean absolute error (MAE) was chosen, with smaller values representing a better fit. A wider frequency range implied a poorer fitting. The shear elasticity  $\mu$  parameters were similar in all ranges, especially for lower values. The shear viscosity  $\eta$  parameters were significantly different between the low frequency range and the high frequency range. Furthermore, to better observe these behaviors, the KV models are represented for each frequency range in Fig. 7. The lines are extrapolated to cover the entire frequency range. In the low frequency range,  $\eta$  was higher for higher concentrations, implying that the high frequency range behavior could not be captured. On the contrary, the high frequency range  $\eta$  was able to satisfactorily capture the low frequency range behavior.

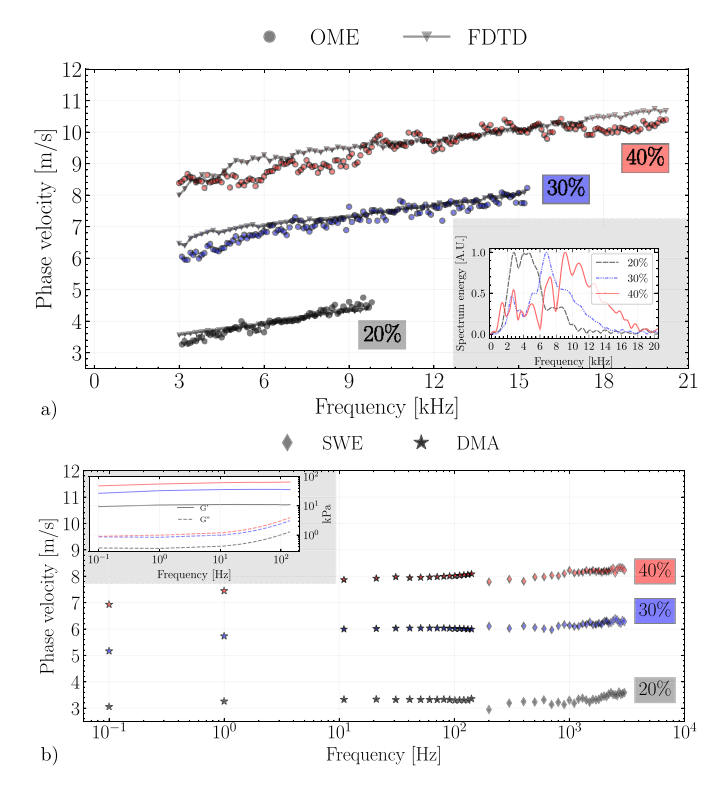


**Fig. 6.** Experimental dispersion curves. (a) The high frequency phase velocity values estimated from optical micro-elastography (OME) and simulations (FDTD). The right inset displays the energy frequency content for each concentration of PAM. (b) The low frequency phase velocity values estimated from Dynamic Mechanical Analysis (DMA) and Shear Wave Elastography (SWE). The frequency axis is represented in log scale. The inset represents the storage G' and loss G'' moduli on a log-log scale.

In Table 3, the KV parameters are used to explore the cutoff frequencies. First, we calculated on the left side the values of the frequency regime  $(\omega\tau)$  considering the upper frequency limits and the relaxation

Table 2

KV model parameters (shear elasticity and viscosity) fitted to each PAM concentration and frequency range. Data presented as mean ± standard deviation. LF: low frequency, HF: high frequency, WF: whole frequency. MAE: Mean Absolute Error.

PAM concentration (%)	LF			HF			WF		
	μ (kPa)	η (Pa s)	MAE (m/s)	μ (kPa)	η (Pa s)	MAE (m/s)	μ (kPa)	η (Pa s)	MAE (m/s)
40	63.62 ± 11.54	$1.33 \pm 0.21$	0.07	72.52 ± 7.85	$0.51 \pm 0.12$	0.25	69.94 ± 8.07	$0.53 \pm 0.06$	0.25
30	$37.52 \pm 7.01$	$0.61 \pm 0.18$	0.07	$40.40 \pm 5.04$	$0.41 \pm 0.12$	0.17	$39.21 \pm 3.28$	$0.43 \pm 0.07$	0.16
20	$10.26 \pm 3.10$	$0.34 \pm 0.04$	0.06	$10.68 \pm 2.29$	$0.21 \pm 0.09$	0.09	$10.81 \pm 0.53$	$0.21~\pm~0.02$	0.09

Table 3 KV frequency regimes and prediction of high cutoff frequencies using  $\omega \tau = 1$ . LF: low frequency, HF: high frequency, WF: whole frequency.  $f_c$ : cutoff frequency.

PAM concentration (%)	LF		HF		WF	WF	
	ωτ	$\omega \tau = 1$ $f_c \text{ [kHz]}$	ωτ	$\omega \tau = 1$ $f_c$ [kHz]	$\overline{\omega \tau}$	$\omega \tau = 1$ $f_c$ [kHz]	
40	0.59	7.6	0.89	22.6	0.96	21.0	
30	0.38	9.8	0.97	15.7	1.05	14.5	
20	0.62	4.8	1.21	8.0	1.19	8.2	

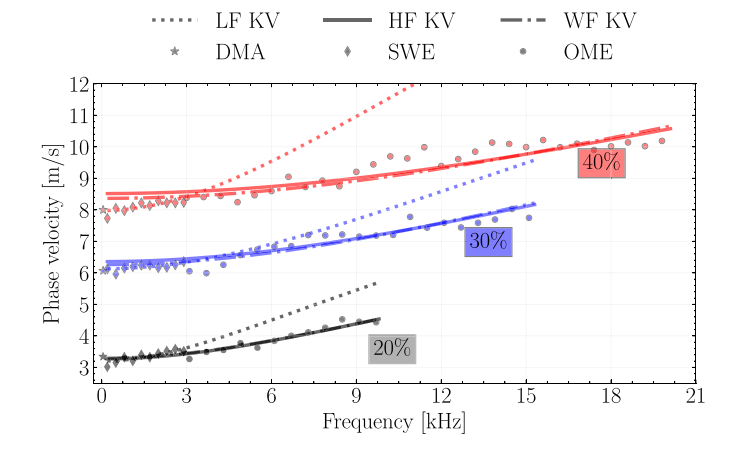


Fig. 7. KV fitting to experimental data in different frequency ranges. The low frequency range (LF) corresponds to DMA+SWE, while the high frequency range (HF) corresponds to OME. The whole frequency range is the combination of the previous ranges (WF = LF + HF). Fewer experimental points are plotted for the sake of clarity.

times estimated from the experimental results. It can be seen that in the low frequency range,  $\omega \tau$  is in all cases less than 1, while in the other ranges it is around 1. On the right side, high cutoff frequencies were calculated assuming  $\omega \tau = 1$ . Given the overestimation of the viscous parameter in the low frequency range, the cutoff frequency was underestimated. In the other ranges, a fair approximation was obtained with respect to the limits that were reached when calculating the phase velocity.

#### 4.4. Spatial analysis of the mode of wave propagation

The series of sequential snapshots in Fig. 8a show that the longitudinal shear waves captured had a spherical front due to the circular geometry of the magnet. We analyzed the propagated waves to confirm that they did not form part of complex modes of guided propagation. The tested samples had a thickness larger (4.5 mm) than the maximum  $\lambda$ . The same applies to the SWE measurements, where the maximum  $\lambda$  was around 20 mm in the 40% PAM, and the sample thickness was 50 mm. As displayed in Fig. 8a, the minimum wavelength is 0.517 mm for the 40% PAM, 0.502 mm for the 30% PAM, and 0.451 mmm for the 20% PAM, in OME measurements. This can in fact be verified in the snapshots shown in the same figure.

To verify that the previous minimum  $\lambda$  did not limit the resolution of the system, wave propagation at high frequencies from a hard to a soft medium was explored. In the bilayer sample (shown in Fig. 8b)

the straight transition plane has a constant length of 0.3 mm. When the wave traveled through this plane, there was an abrupt alteration in its front due to a change in mechanical properties. To see that change, the spatial gradient of the displacement in the same direction of propagation was calculated and plotted in the right hand side image. The length of the lateral distance of the gradient (marked between the white lines) was approximately 0.3 mm, decreasing slightly as the frequency increased.

#### 5. Discussion

In this study, OME was presented as a feasible technique for obtaining a reliable viscoelastic analysis over an ultrawide frequency range. To achieve micrometer resolutions and avoid guided wave propagation, a high frequency excitation was used, and the detecting capabilities of the imaging system were enhanced.

A magnetically based excitation without direct mechanical contact was proposed. This method of excitation provided high-efficiency transmission between the input excitation frequency and the medium displacement. This remote generation of shear waves by means of the Lorentz force has already been explored [40,41]. In contrast to these previous studies, where the waves generated had a low frequency response (<1 kHz), here the motion of the magnet allowed it to reach higher frequency (>3 kHz). A chirp-type signal provided a uniform magnitude throughout the frequency sweep, which was convenient for achieving a continuous dispersion curve, as well as a higher SNR than an impulse [42]. When the magnet began to vibrate, it first had to overcome the inertia of the medium that was holding it. At high frequency, the inductance of the coil reduces the current developed in the coil, which directly affects the magnetic force. Therefore, to beat the inertia, a continuous frequency sweep starting at lower frequencies guaranteed to observe wave displacements beyond 20 kHz. When the excitation started at low frequencies (<3 kHz), the magnet vibration was slow and had a large amplitude, and high frequencies could not be developed. To achieve a balance and avoid guided waves due to large  $\lambda$ , the input signal started at 5 kHz. Even so, enough information was obtained to reconstruct the velocity at frequencies lower than the excitation, starting at 3 kHz. This was because in the transition from standing to moving, lower frequency components were generated. The shape of the wavefront can be changed with the geometry of the embedded magnet. In our case, a circular geometry facilitated the study of the excitation force as a result of the assumptions made about the eddy current. By replacing the magnet by a metal plate, such as aluminum, the maximum magnetic force was reduced by 85%, and we did not observe any motion or propagating wave. This meant that the permanent magnetic field provided the force necessary to move the disk within the medium. To further increase this force, a magnet

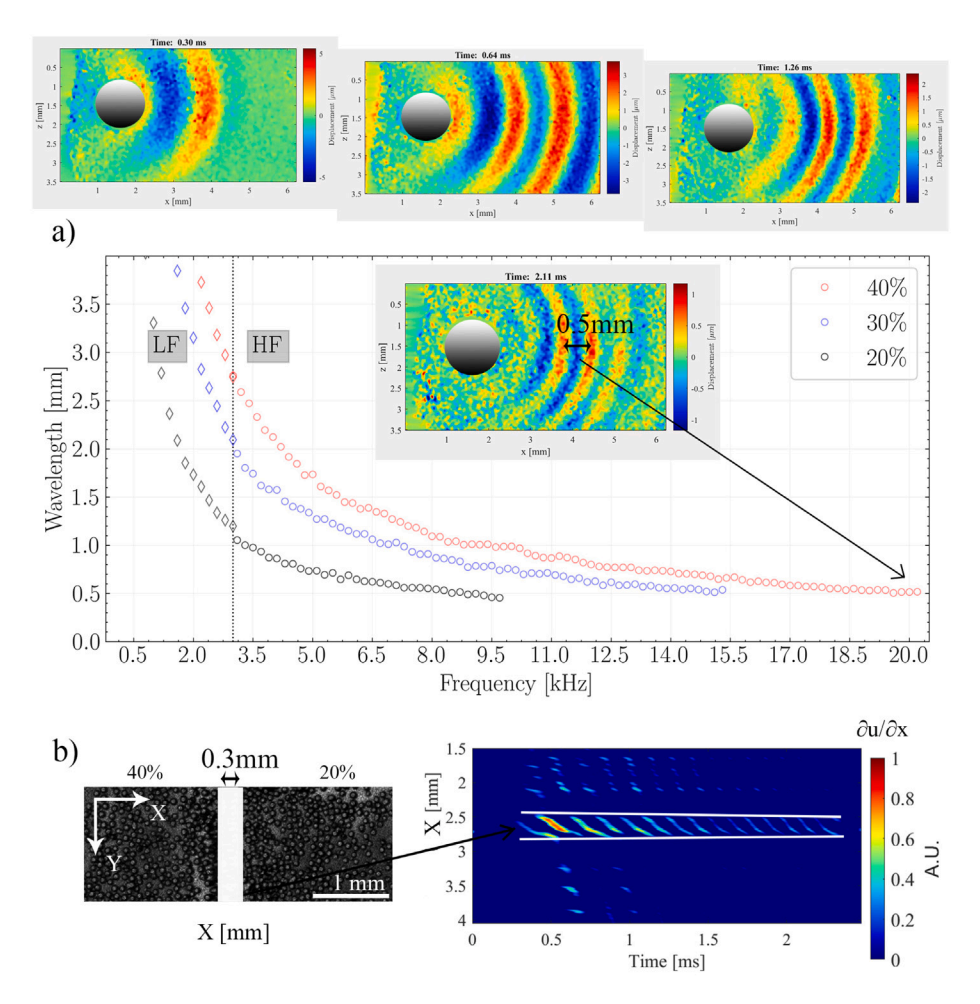


Fig. 8. (a) Sequential snapshots of the longitudinal shear wave propagating in the 40% PAM showing the horizontal component (X) of the particle displacement after optical flow reconstruction. The plot shows the decreasing wavelength as the excitation reached higher frequencies. (b) Image of the transition between two concentrations (bilayer) and the spatial gradient of displacement when the wave propagated in the white rectangle (transition zone).

with a higher permanent field can be used, such as NdFeB-52, and the input current can be increased. Besides, strong magnetic fields are biologically harmless [24].

Techniques using high speed cameras have found a niche application in gaining greater insight into the physics of wave propagation and some of its limits [6,17]. Its advantages are the high acquisition rate and spatial resolution, which allow small displacements to be captured in short times. By exploring the propagation in the immediate vicinity of the excitation area, it is possible to capture some wavelengths at high frequencies that attenuate quickly. To obtain an accurate displacement field, the algorithm used to calculate the dense optical flow presented a problem. If excitation frequencies lower than 3 kHz were used, the displacements would be greater than 10  $\mu m$ . Due to the large amplitude of vibration of the magnet to generate this displacement, the sample was lifted off the base. This changed the illumination conditions, and the results were erroneous.

The tests on the bilayer samples proved that it was the resolution of the imaging system that limited the accuracy of the displacement field reconstruction. The minimum  $\lambda$  was 0.451 mm, and we could detect a transition of 0.3 mm. As discussed in [7], the use of minimum windows or propagation distances for velocity estimations decreases the final resolution. Blurred and irregular transitions have been frequently observed [2]. The camera resolution can be increased by using a microscopic lens, which can provide a resolution of less than  $1\times 1~\mu m^2.$  However, the generated displacement amplitude would have to be decreased to be captured in the field of view, which at high frequencies might mean no motion.

With this setup, waves traveling at the speed of shear waves (a few m/s) and with a longitudinal displacement were observed. Longitudinal shear waves have already been used in optical coherence elastography with satisfactory results [43,44]. To confirm the shear wave nature of these observed longitudinal waves, the group velocity was measured in the lateral plane shown in Fig. 4b. A value of 9.4 m/s was obtained for the 40% concentration sample, which was in the range of its dispersion curve. The geometrical diffraction due to the spherical front did not seem to affect the phase information in the frequency domain. We compared the velocity values with and without spherical front corrections, and the differences were all below 5%. The changes in the shape of the dispersion curve (Fig. 6a) at specific frequency intervals can be caused by various factors, such as high attenuation or inhomogeneous particle distribution. This meant that in the ROI chosen, the propagation front was not completely homogeneous. In the case of SWE, it was necessary to stir the graphite during curing to prevent it from settling at the bottom, while for OME in some cases there were gaps or a higher density of particles due to the fabricating process.

Several results were used to confirm that the dispersive behavior of the shear waves measured with OME was not sensitive to the geometrical conditions of the medium. First, the (f,k) space gave information on how the propagation was distributed spatially and temporally. Its magnitude revealed that only one propagation mode was captured. When there are other modes, additional information appears that deviates from the dominant mode [32,42]. In our case, we did not apply any amplitude mask, and consequently, the measurement data at some points had some apparent noise or artifact. Secondly, given

the boundary conditions of the experiment, the potential lowest-order Lamb waves would propagate along the surface, known as Rayleigh waves. The simulation results in the lateral plane allowed one to see the ratio of amplitudes between the displacements at the midline of the medium and at the border. The energy near the edges was found to be four times lower than in the midline. In addition, the high attenuation together with the geometrical dispersion caused the possible effects of this surface wave on the dominant mode to be negligible. Third, the thickness of the samples (4.5 mm) was greater than the wavelength in the frequency range studied. In the worst case, for each PAM concentration (at 3 kHz), the wavelength was 2.7, 2.0, and 1.0 mm, for 1.0%, 0.5%, and 0.25%, respectively. These values decreased rapidly with frequency. Similarly, the values obtained by SWE consistently follow the dispersion curve toward low frequencies, and in this case the thickness of the samples (50 mm) was much greater than  $\lambda$  in the frequency range. With these arguments, the possibility that the captured mode was a Rayleigh wave was ruled out. Therefore, they were considered bulk shear waves whose frequency dependence was attributed to the material dispersion and not to the waveguide dispersion.

The manufactured PAM hydrogels are considered linear elastic materials [45], and as such we had to add glycerol to increase the viscosity [46]. In the literature, this material had not been characterized at such high concentrations and, in any case, without ingredients that add viscosity. For the 20% PAM, the shear modulus has been found between 8 and 12 kPa [27,45], which is similar to our DMA results. The difference between values has been attributed to crosslinker concentration, polymerization temperature, and swelling equilibrium [47]. In our case, we used a 5% crosslinker, reaching a maximum temperature reaction of 42  $^{\circ}$ C, and we let the medium undisturbed for 30 min in water before measuring.

Some considerations that may limit the scalability of the proposed method include the need for transparency of the medium and the need for embedding the magnet in the sample to be measured. Although the OME technique can achieve a fine spatial resolution, it is not comparable to nanometric resolution techniques such as Atomic Force Microscopy (AFM) or Brillouin microscopy. However, this situation can be advantageous for some applications. Exploring the mechanical behavior of a material beyond the low frequency or quasi-static regimes, such as those provided by AFM, will allow us to understand its response to a full range of dynamic mechanical stimuli. This is relevant, for example, in regenerative medicine. Measurement of the viscoelasticity of the culture substrate provides information on its ability to support cell migration and its potential to induce cell differentiation [48]. PAM hydrogels have been a popular choice for studying cell-substrate mechanical interactions [49]. On the one hand, this is due to the wide achievable range of mechanical properties by varying its concentration. Optimization of mechanical parameters increases the efficiency of culture systems. On the other hand, its total transparency facilitates visualization of cellular processes. With the OME technique, a wide spectrum of viscoelastic properties could be obtained from this type of media. By separating the plane in which measurements are taken from the plane in which the cells are seeded, the properties could be monitored over time without disrupting the cells. A confocal lens would provide at the same time an imaging system for mechanical characterization and an observing system for cellular reactions.

We demonstrated that techniques available for mechanical characterization, such as SWE and DMA, agreed well with OME's phase velocity. The rheological agreement was also studied according to the frequency range. Simple rheological models, such as the KV model, are based on single relaxation processes, which are not representative of many multiscale materials and biological structures [50]. Still, it has been shown in hydrogels, such as gelatin and agar [17,51], and here in PAM, that they can be well described by this type of model. In the case of other models, such as Maxwell, its plateau behavior at high frequencies would not accurately describe the observed dispersive

response. For more complex models, such as Zener, where an additional elastic term is added, the interpretation of multiple relaxation times is no longer straightforward.

A problem arose when taking a reduced dispersion curve to fit the KV model, since the estimated rheological parameters showed high variability. By comparing the low frequency range (<3 kHz) with the high frequency range (>3 kHz), for  $\mu$  the relative errors were less than 10%, but for  $\eta$  the errors reached 60% and they can be higher with a higher dispersive behavior. By using a wide frequency bandwidth dispersion curve for the rheological parameter, the response from quasistatic to cutoff frequency was successfully modeled. Furthermore, to verify the robustness of the fittings, several initial guess values were randomly chosen. For  $\mu$  between 1 and 100 kPa and for  $\eta$  between 0.05 and 2 Pa s. All converged to the values shown with a variation of less than 5%

The calculated cutoff frequencies shown in Table 3 only depended on the rheological parameters. This can be interpreted from another physical point of view. If the excitation frequency is higher than the relaxation time, the material does not have time to relax and respond, that is, to vibrate at that frequency. Therefore, the propagation energy at these frequencies is diffused. The differences between theory and experiments were mainly attributed to experimental setup and reconstruction algorithms. On the other hand, attenuation increases exponentially with distance. At one wavelength, the amplitude decreases by  $e^{\alpha\lambda}$ , with  $\alpha$  the attenuation factor. The inverse of the attenuation per wavelength (A) measures the distance in number of wavelengths, when the amplitude decays close to the noise level. For low frequencies, the KV model approaches  $A \approx \pi \omega \tau$  [35]. If the limit is set to  $\omega \tau = 1$ , as observed in Table 3, then  $A = \pi$ , thus  $A^{-1} = 0.318\lambda$ . If the propagation distance is less than one third of a wavelength, no waves will propagate. This result was in line with the expression proposed by Laloy et al. [17].

#### 6. Conclusions

The proposed micro-elastography technique was validated. A setup for generating and imaging high frequency shear waves with enough spatial and temporal resolution was configured. Few studies on elastography have reached such high frequencies and even fewer have observed ultrasonic shear waves in soft media. Tracking the displacements close to the excitation area with high resolution and without near-field effects was key to reaching the cutoff frequencies, since at such short propagation distances other methods are technically limited. The combination of the three measurement techniques provided rheology information over 6 orders of magnitude of frequencies. The study at different frequencies of a simple rheological model such as KV yielded interesting conclusions. There was no good agreement on the viscous parameter if the measurements were made at low frequencies (SWE range) and extrapolated to higher frequencies. A wide dispersion curve was necessary for the rheology to be well interpreted. This led us to hypothesize that in viscoelastic and homogeneous materials that follow a KV model over their entire measurable frequency range, the KV model was capable of predicting the high frequency cutoff. As a potential application, the mechanical characterization of tissue engineering scaffolds is envisioned.

#### CRediT authorship contribution statement

Jorge Torres: Data curation, Formal analysis, Writing – original draft, Investigation, Methodology. Antonio Callejas: Software, Validation. Antonio Gomez: Validation, Writing – review & editing. Guillermo Rus: Supervision, Funding acquisition.

#### **Declaration of competing interest**

The authors declare that they have no known competing financial interests or personal relationships that could have appeared to influence the work reported in this paper.

#### Data availability

Data will be made available on request

#### Acknowledgments

The authors would like to thank R. Muñoz for illuminating discussions on magnetism.

This research was funded by Ministerio de Educación, Cultura y Deporte, Spain grant numbers DPI2017-83859-R, and EQC2018-004508-P; Ministerio de Ciencia e Innovación, Spain grant numbers PID2020-115372RB-I00, PYC20 RE 072 UGR; Ministerio de Sanidad, Servicios Sociales e Igualdad, Spain grant numbers DTS15/00093 and PI16/00339; Instituto de Salud Carlos III y Fondos Feder, Spain; Junta de Andalucía, Spain grant numbers PI-0107-2017, PIN-0030-2017 and IE2017-5537; P21-00182 Consejería de Universidad, Investigación e Innovación de la Junta de Andalucía; MCIN/AEI 10.13039/501100011 033 grant number PRE2018-086085 (Co-funded by European Social Fund "Investing in your future"); Consejería de economía, conocimien to, empresas y universidad and European Regional Development Fund (ERDF) SOMM17/6109/UGR, B-TEP-026- IE2017-5537 and P18-RT-1653.

#### References

- [1] K.M. Kennedy, L. Chin, R.A. McLaughlin, B. Latham, C.M. Saunders, D.D. Sampson, B.F. Kennedy, Quantitative micro-elastography: imaging of tissue elasticity using compression optical coherence elastography, Sci. Rep. 5 (1) (2015) 1–12.
- [2] X. Qian, T. Ma, M. Yu, X. Chen, K.K. Shung, Q. Zhou, Multi-functional ultrasonic micro-elastography imaging system, Sci. Rep. 7 (1) (2017) 1–11.
- [3] K. Haase, A.E. Pelling, Investigating cell mechanics with atomic force microscopy, J. R. Soc. Interface 12 (104) (2015).
- [4] C. Alibert, B. Goud, J.B. Manneville, Are cancer cells really softer than normal cells? Biol. Cell 109 (5) (2017) 167–189.
- [5] M.S. Hepburn, M.S. Hepburn, P. Wijesinghe, P. Wijesinghe, P. Wijesinghe, L.G. Major, J. Li, J. Li, J. Li, A. Mowla, A. Mowla, C. Astell, H.W. Park, Y. Hwang, Y. Hwang, Y.S. Choi, B.F. Kennedy, B.F. Kennedy, B.F. Kennedy, Three-dimensional imaging of cell and extracellular matrix elasticity using quantitative micro-elastography, Biomed. Opt. Express 11 (2) (2020) 867–884.
- [6] A. Zorgani, T.A. Ghafour, M. Lescanne, S. Catheline, A. Bel-Brunon, Optical elastography: tracking surface waves with digital image correlation, Phys. Med. Biol. 64 (5) (2019) 055007.
- [7] C. Zemzemi, A. Zorgani, L. Daunizeau, S. Belabhar, R. Souchon, S. Catheline, Super-resolution limit of shear-wave elastography, Europhys. Lett. 129 (3) (2020) 34002.
- [8] M.A. Kirby, K. Zhou, J.J. Pitre, L. Gao, D.S. Li, I.M. Pelivanov, S. Song, C. Li, Z. Huang, T.T. Shen, et al., Spatial resolution in dynamic optical coherence elastography, J. Biomed. Opt. 24 (9) (2019) 096006.
- [9] G.Y. Li, Y. Zheng, Y.X. Jiang, Z. Zhang, Y. Cao, Guided wave elastography of layered soft tissues, Acta Biomater. 84 (2019) 293–304.
- [10] T. Deffieux, J.-L. Gennisson, J. Bercoff, M. Tanter, On the effects of reflected waves in transient shear wave elastography, IEEE Trans. Ultrason. Ferroelectr. Fro. Control 58 (10) (2011) 2032–2035.
- [11] N. Sasaki, Viscoelastic properties of biological materials, in: Viscoelasticity From Theory to Biol. Appl., 2012.
- [12] H. Li, G. Flé, M. Bhatt, Z. Qu, S. Ghazavi, L. Yazdani, G. Bosio, I. Rafati, G. Cloutier, Viscoelasticity imaging of biological tissues and single cells using shear wave propagation, Front. Phys. 9 (2021) 350.
- [13] K. Zhang, M. Zhu, E. Thomas, S. Hopyan, Y. Sun, Existing and potential applications of elastography for measuring the viscoelasticity of biological tissues in vivo, Front. Phys. 9 (2021) 294.
- [14] G. Rus, I.H. Faris, J. Torres, A. Callejas, J. Melchor, Why are viscosity and nonlinearity bound to make an impact in clinical elastographic diagnosis? Sensors 20 (8) (2020) 2379.
- [15] E.L. Carstensen, K.J. Parker, Physical models of tissue in shear fields, Ultrasound Med. Biol. 40 (4) (2014) 655–674.
- [16] P. Kijanka, M.W. Urban, Phase velocity estimation with expanded bandwidth in viscoelastic phantoms and tissues, IEEE Trans. Med. Imaging 40 (5) (2021) 1352–1362.
- [17] G. Laloy-Borgna, A. Zorgani, S. Catheline, Micro-elastography: Toward ultrasonic shear waves in soft solids, Appl. Phys. Lett. 118 (11) (2021) 113701.
- [18] R.M. Sigrist, J. Liau, A.E. Kaffas, M.C. Chammas, J.K. Willmann, Ultrasound elastography: Review of techniques and clinical applications, Theranostics 7 (5) (2017) 1303–1329.

- [19] Y.K. Mariappan, K.J. Glaser, R.L. Ehman, Magnetic resonance elastography: a review, Clin. Anat. 23 (5) (2010) 497–511.
- [20] A. Sarvazyan, T.J. Hall, M.W. Urban, M. Fatemi, S.R. Aglyamov, B.S. Garra, An overview of elastography-an emerging branch of medical imaging, Curr. Med. Imaging Rev. 7 (4) (2011) 255–282.
- [21] R. Righetti, S. Srinivasan, J. Ophir, Lateral resolution in elastography, Ultrasound Med. Biol. 29 (5) (2003) 695–704.
- [22] S.J. Backhaus, G. Metschies, M. Billing, J. Schmidt-Rimpler, J.T. Kowallick, R.J. Gertz, T. Lapinskas, E. Pieske-Kraigher, B. Pieske, J. Lotz, et al., Defining the optimal temporal and spatial resolution for cardiovascular magnetic resonance imaging feature tracking, J. Cardiovasc. Magn. Reson. 23 (1) (2021) 1–12.
- [23] P. Grasland-Mongrain, A. Zorgani, S. Nakagawa, S. Bernard, L.G. Paim, G. Fitzharris, S. Catheline, G. Cloutier, Ultrafast imaging of cell elasticity with optical microelastography, Proc. Natl. Acad. Sci. 115 (5) (2018) 861–866.
- [24] J.F. Schenck, Safety of strong, static magnetic fields, J. Magn. Reson. Imaging 12 (1) (2000) 2–19.
- [25] A.P. Sarvazyan, M.W. Urban, J.F. Greenleaf, Acoustic waves in medical imaging and diagnostics, Ultrasound Med. Biol. 39 (7) (2013) 1133–1146.
- [26] K.R. Nightingale, M.L. Palmeri, R.W. Nightingale, G.E. Trahey, On the feasibility of remote palpation using acoustic radiation force, J. Acoust. Soc. Am. 110 (1) (2001) 625–634.
- [27] M.J. Choi, S.R. Guntur, K.I. Lee, D.G. Paeng, A. Coleman, A tissue mimicking polyacrylamide hydrogel phantom for visualizing thermal lesions generated by high intensity focused ultrasound. Ultrasound Med. Biol. 39 (3) (2013) 439–448.
- [28] J.-L. Gennisson, A. Marcellan, A. Dizeux, M. Tanter, Rheology over five orders of magnitude in model hydrogels: agreement between strain-controlled rheometry, transient elastography, and supersonic shear wave imaging, IEEE Trans. Ultrason. Ferroelectr. Freq. Control 61 (6) (2014) 946–954.
- [29] S. Catheline, N. Benech, Longitudinal shear wave and transverse dilatational wave in solids, J. Acoust. Soc. Am. 137 (2) (2015) EL200–EL205.
- [30] G. Farnebäck, Two-frame motion estimation based on polynomial expansion, in: Lect. Notes Comput. Sci. (Including Subser. Lect. Notes Artif. Intell. Lect. Notes Bioinformatics), Vol. 2749, Springer, Berlin, Heidelberg, 2003, pp. 363–370.
- [31] T. Loupas, J. Powers, R.W. Gill, An axial velocity estimator for ultrasound blood flow imaging, based on a full evaluation of the Doppler equation by means of a two-dimensional autocorrelation approach, IEEE Trans. Ultrason. Ferroelectr. Freq. Control 42 (4) (1995) 672–688.
- [32] M. Bernal, I. Nenadic, M.W. Urban, J.F. Greenleaf, Material property estimation for tubes and arteries using ultrasound radiation force and analysis of propagating modes, J. Acoust. Soc. Am. 129 (3) (2011) 1344.
- [33] A.Y. Malkin, A.I. Isayev, Rheology: Concepts, Methods, and Applications, Elsevier, 2022.
- [34] R. Fletcher, Practical Methods of Optimization: Vol. 2: Constrained Optimization, JOHN WILEY & SONS, INC., ONE WILEY DR., SOMERSET, N. J. 08873, 1981, 1981, 224.
- [35] S. Holm, Waves with Power-Law Attenuation, Springer, 2019.
- [36] A. Callejas, J. Melchor, I.H. Faris, G. Rus, Viscoelastic model characterization of human cervical tissue by torsional waves, J. Mech. Behav. Biomed. Mater. 115 (2021) 104261.
- [37] A. Callejas, A. Gomez, I.H. Faris, J. Melchor, G. Rus, Kelvin-Voigt parameters reconstruction of cervical tissue-mimicking phantoms using torsional wave elastography, Sensors 19 (15) (2019) 3281.
- [38] J. Bamber, D. Cosgrove, C.F. Dietrich, J. Fromageau, J. Bojunga, F. Calliada, V. Cantisani, J.-M. Correas, M. D'onofrio, E. Drakonaki, et al., EFSUMB guidelines and recommendations on the clinical use of ultrasound elastography. Part 1: Basic principles and technology, Ultraschall Med.-Eur. J. Ultrasound 34 (02) (2013) 169–184.
- [39] D. Meeker, Finite element method magnetics, FEMM 4 (32) (2010) 162.
- [40] Z. Sun, B. Giammarinaro, A. Birer, G. Liu, S. Catheline, Shear wave generation by remotely stimulating aluminum patches with a transient magnetic field and its preliminary application in elastography, IEEE Trans. Biomed. Eng. 68 (7) (2020) 2129–2139.
- [41] P. Grasland-Mongrain, E. Miller-Jolicoeur, A. Tang, S. Catheline, G. Cloutier, Contactless remote induction of shear waves in soft tissues using a transcranial magnetic stimulation device, Phys. Med. Biol. 61 (6) (2016) 2582.
- [42] A. Ramier, B. Tavakol, S.-H. Yun, Measuring mechanical wave speed, dispersion, and viscoelastic modulus of the cornea using optical coherence elastography, Opt. Express 27 (12) (2019) 16635–16649.
- [43] J. Zhu, J. Yu, Y. Qu, Y. He, Y. Li, Q. Yang, T. Huo, X. He, Z. Chen, Coaxial excitation longitudinal shear wave measurement for quantitative elasticity assessment using phase-resolved optical coherence elastography, Opt. Lett. 43 (10) (2018) 2388–2391.
- [44] F. Zvietcovich, R.G. Gary, H. Mestre, M. Giannetto, M. Nedergaard, J.P. Rolland, K.J. Parker, Longitudinal shear waves for elastic characterization of tissues in optical coherence elastography, Biomed. Opt. Express 10 (7) (2019) 3699–3718.
- [45] A.K. Denisin, B.L. Pruitt, Tuning the range of polyacrylamide gel stiffness for mechanobiology applications, ACS Appl. Mater. Interfaces 8 (34) (2016) 21893–21902.
- [46] A. Sharma, S.G. Marapureddy, A. Paul, S.R. Bisht, M. Kakkar, P. Thareja, K.P. Mercado-Shekhar, Characterizing viscoelastic polyvinyl alcohol phantoms for ultrasound elastography, Ultrasound Med. Biol. 49 (2) (2023) 497–511.

- [47] V. Damljanovic, B. Christoffer Lagerholm, K. Jacobson, Bulk and micropatterned conjugation of extracellular matrix proteins to characterized polyacrylamide substrates for cell mechanotransduction assays, Biotechniques 39 (6) (2005) 847–851.
- [48] A.J. Engler, F. Rehfeldt, S. Sen, D.E. Discher, Microtissue elasticity: measurements by atomic force microscopy and its influence on cell differentiation, Methods Cell Biol. 83 (2007) 521–545.
- [49] C.E. Kandow, P.C. Georges, P.A. Janmey, K.A. Beningo, Polyacrylamide hydrogels for cell mechanics: steps toward optimization and alternative uses, Methods Cell Biol. 83 (2007) 29–46.
- [50] K. Parker, T. Szabo, S. Holm, Towards a consensus on rheological models for elastography in soft tissues, Phys. Med. Biol. 64 (21) (2019) 215012.
- [51] S. Catheline, J.-L. Gennisson, G. Delon, M. Fink, R. Sinkus, S. Abouelkaram, J. Culioli, Measurement of viscoelastic properties of homogeneous soft solid using transient elastography: An inverse problem approach, J. Acoust. Soc. Am. 116 (6) (2004) 3734–3741.